Broadband Ptychotomography with a Hyperspectral Detector

Wiebe Stolp,[1,*] Frederic van Assche,[1] Ruizhi Tang,[1] Karel Desplenter,[1] Caori Organista Castelblanco,[1]
Ralf Ziesche,[2] Silvia Cipiccia,[3] Darren Batey,[4] and Matthieu N. Boone[1,†]
[1]*UGCT-RP, Department of Physics and Astronomy, Ghent University, Ghent 9000, Belgium*
[2]*Helmholtz-Zentrum Berlin, Hahn-Meitner-Platz 1, 14109 Berlin, Germany*
[3]*Department of Medical Physics and Biomedical Engineering, University College London,*
London WC1E 6BT, United Kingdom
[4]*Diamond Light Source, Harwell Science and Innovation Campus,*
Fermi Avenue, Didcot OX11 0DE, United Kingdom

(Received 15 November 2024; accepted 2 May 2025; published 27 June 2025)

X-ray ptychography is a robust microscopy technique with nanoscale resolution that requires a spatially and temporally coherent illumination. In a typical setup, the temporal coherence requirements are satisfied by monochromating the x-ray source, e.g., using a crystal monochromator. Recent studies have shown that energy resolving, or hyperspectral, detectors can to some extent replace the role of the monochromator to perform, e.g., edge-subtraction ptychographic imaging with broadband radiation in a single acquisition. Scaling this capability from two dimensions (2D) to three dimensions (3D), and from a single absorption edge to multiple edges, is critical for its applications in structural and elemental characterisation. The method is hitherto limited by the inherently lower maximum count rate of hyperspectral detectors and the chromaticity of the optics often used in x-ray ptychography experiments, namely Fresnel zone plates. In this work, we design an optimized broadband spectroscopic ptychography setup and use it to perform 3D hyperspectral imaging of particles of battery material containing various percentages of nickel, manganese, cobalt (NMC). We show that we can identify different compositions based on their spectral response. We discuss the results and provide guidelines for future exploitation of the method in laboratory settings.

DOI: 10.1103/kbrf-gb9c

X-ray ptychography [1,2] is a lensless microscopy technique that can provide nanoscale resolution and large fields of view and can be viewed as a combination of scanning transmission x-ray microscopy (STXM) and coherent diffraction imaging (CDI) [3]. In a ptychographic acquisition, diffraction data are recorded by an array detector placed in the far field while scanning a sample through a small coherent illumination profile called the *probe*. A schematic of a typical x-ray ptychography setup is shown in Fig. 1. Given sufficient probe overlap between subsequent steps, an iterative reconstruction algorithm can retrieve a complex valued transmission image of the sample that encodes the phase shift and attenuation properties, as well as a complex image of the probe.

Ptychography and standard CDI are theoretically diffraction limited [4] and, therefore, not ultimately limited in

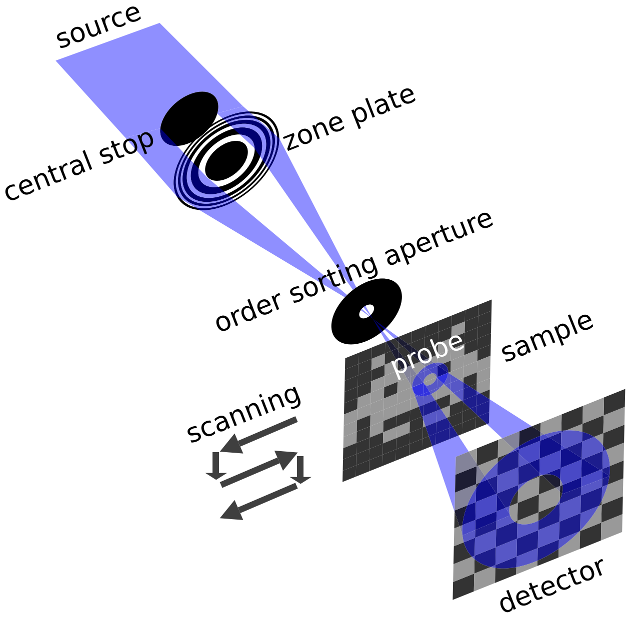

FIG. 1. Typical experimental setup for ptychography: a Fresnel zone plate diffractive lens is used to create a diverging wavefront that hits the sample after focus. The combination of a central stop and order sorting aperture isolates the first diffraction order (in blue) from the unwanted diffraction orders (not shown).

---

[*] Contact author: wiebestolp@gmail.com

[†] Contact author: matthieu.boone@ugent.be

resolution by the probe size, as is the case for STXM, or detector pixel size and magnification, as is the case for direct imaging. Moreover, since an algorithm is used instead of a lens to form an image, they are not affected by lens aberrations. Furthermore, unlike standard CDI, ptychography does not rely on prior information about the illumination due to its ability to retrieve an image of the probe. X-ray ptychography relies on coherent radiation, and temporal coherence is usually achieved through spectral filtering with a crystal monochromator. This filtering is highly inefficient as most of the spectrum is discarded. For this reason highly brilliant x-ray sources, i.e., synchrotrons, are needed in order to perform x-ray ptychography within reasonable time frames. However, it has recently been demonstrated that sufficient temporal coherence for ptychography can also be achieved by using a hyperspectral detector instead of a monochromator [5]. Hyperspectral detectors are imaging detectors capable of accurately resolving the energy of a photon in addition to its location of incidence in the two-dimensional (2D) detector active area. An acquisition with a hyperspectral detector can be organized into a datacube with two spatial dimensions and one spectral dimension. With such a detector the temporal coherence becomes tunable (within the limits of the detector's energy resolution) and attainable in postprocessing by slicing and summing the data along the spectral dimension. This not only enables ptychography without a monochromator, but also the simultaneous acquisition of ptychographic data across a broad spectrum, which can conventionally only be achieved by scanning the monochromator energy. As such, the structural information provided by ptychography can be coupled with a sensitivity to elemental composition through the localized spectral response of the sample, e.g., via edge subtraction, as shown in a previous work [5]. This elemental sensitivity is of high interest in many research areas, ranging from catalysis [6] to biology [7].

Our earlier proof-of-concept broadband acquisition setup [5] had three main limitations. First, current hyperspectral detectors have a relatively low flux tolerance compared to photon counting detectors, requiring longer exposure times for similar photon statistics. Second, the chromatic nature of the 400 μm diameter Fresnel zone plate (FZP), used to focus the beam upstream of the sample, causes the probe size to vary drastically across the broadband spectrum. The probe size is an important parameter in ptychographic sampling theory and is related to other experimental parameters. Naturally, the larger the probe, the fewer scan positions are required for sufficient probe overlap. However, a larger probe also creates finer spatial frequencies in the far field diffraction patterns; therefore, through diffractive sampling theory, the maximum acceptable probe size in the spectrum is bounded by the geometry (i.e., the propagation distance and detector pixel pitch). However, the smallest probe in the spectrum still dictates the ptychographic step size for the whole experiment. As a result, for a given geometry, significantly more steps are required when using broadband radiation than when using monochromatic radiation. This ultimately increases the scan duration through the overhead that exists with each scan step. One could increase the size of all probes by moving the sample closer to the detector and employ detector upsampling [8], an algorithmic adaptation that allows one to deal with oversized probes, but this does not solve the problem since this method also relies on a reduced step size. Furthermore, since the energy bins selected and summed for ptychographic reconstruction will always be finite in size, and not infinitesimal, a slowly varying probe size will be modeled better by a reconstruction algorithm that treats each individual energy bin as if it were monochromatic. Here the minimum required energy bin size for satisfactory reconstructions depends on acquisition time through photon statistics. Therefore, in two different ways, the probe size variation results in an increased total scan duration, in addition to the increase already caused by the detector flux tolerance. These problems combined have so far prevented performing three-dimensional (3D) hyperspectral ptychography.

To solve them, we have designed a new setup based on a small diameter FZP, which reduces its chromaticity in the context of ptychography [9], and consequently broadens the spectrum that can be covered simultaneously without significantly sacrificing scan speed. Furthermore, it allows for a scan step size that is closer to optimal across the full bandwidth, which finally reduces the total scan duration.

Arguably, an achromatic optics could be used instead, such as Kirkpatrick-Baez (KB) mirrors, but that solution is significantly more expensive than FZPs. Furthermore, since photons outside the region of spectral interest also contribute to the total flux on the detector, this is not necessarily ideal for hyperspectral detectors due to their lower count rate capability. Indeed, in the presence of a spectrum that is broader than necessary, e.g., to perform edge subtraction, the FZP, in combination with an order sorting aperture (OSA), can also act as a bandwidth selector, precisely due to the chromaticity already mentioned. This way filtering does not require an additional optical element. Another downside of achromatic optics is that an ideal probe is in fact not exactly achromatic; the ideal probe size scales with the wavelength. The problem of varying probe sizes in multispectral ptychography is also treated in [10], which used a different approach.

Based on the considerations above, for this experiment, we employed a FZP with a diameter 20 times smaller than the 400 μm diameter FZP used earlier [5] and with a 1.5 times larger numerical aperture. The smaller diameter increases the relative bandwidth over which spectral data can be acquired simultaneously. This effect is proportional to the FZP diameter, i.e., for the same variation in the probe size, an FZP that is 20 times smaller can accept a 20 times larger relative bandwidth. However, the count rate of the

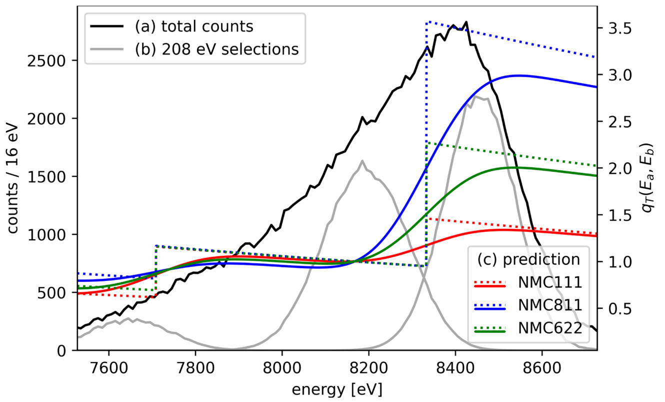

FIG. 2. A collection of spectra relevant for this research. (a) Spectrum, divided in 16 eV bins, as measured by the detector in an empty position of the ptychographic scan. (b) Approximation of the distribution of actual counts in each nominal 208 eV energy bin. (c) The theoretically predicted attenuation coefficient normalized to its value at 8167 eV, i.e., $q(E_a, E_b = 8167\ \text{eV})$. This value is characteristic for each NMC composition. Dotted lines use the original attenuation coefficients; solid lines take into account detection uncertainty (see Appendix A).

detector remains a limiting factor. To exploit its full potential, the size of the FZP's disk illumination on the detector had to be increased to almost match the detector's active area, by changing the beam divergence. This is why this FZP has a larger numerical aperture, resulting from a smaller outermost zone width. For the same reason, the sample-detector distance was almost doubled.

The experiment took place at the I13-1 Coherence beamline [11] at the Diamond Light Source synchrotron facility. The third harmonic of the undulator was centered at 8 keV and broadened by undulator tapering [12]. The other harmonics were filtered out using a combination of a Si mirror and metal filters (950 μm C, 200 μm Al, 30 μm Cu). The horizontal secondary source slits, 210 m upstream of the sample, were closed to 4 μm in order to limit the total flux on the detector. In that same source plane, the vertical source size is 20 μm. The resulting x-ray spectrum as measured by the detector is shown in Fig. 2(a).

A self-standing 10 μm diameter, 80 μm thick cylindrical golden central stop, held in space by 3 fins (Microworks GmbH, Eggenstein-Leopoldshafen, Germany), was placed directly upstream of the small gold FZP (XRnanotech GmbH, Villigen, Switzerland), which is 963 nm thick and has a 20 μm diameter and a 100 nm outer zone, resulting in 50 zones in total.

A 5 μm diameter OSA was placed in the 8 keV FZP focal plane, 12.9 mm downstream of it. The hyperspectral detector is the SLcam pnCCD [13], with an energy resolution measured to be 150 eV FWHM at the Mn Kα fluorescence peak ($E = 5899$ eV) [14], which can be extrapolated to be 180 eV at 8.3 keV assuming $\sqrt{E}$ scaling [15]. It has 264 × 264 pixels with a pixel pitch of 48 μm, and a frame rate of 400 Hz. The detector measures energies by identifying individual photon events through their separation in time and space, causing its accuracy to drop where the pixel occupancy is too high. The limit for this is found to be around 5 photons/pixel/s [16]. Data were acquired using the SpexiDAQ framework [17], which is dedicated to hyperspectral x-ray detectors. The detector was placed 7.8 m downstream of the sample. At this distance the magnified FZP disk intensity profile fills the detector active area completely.

To test the capability of the new setup, we have imaged a sample made of four $\text{Li}(\text{Ni}_x\text{Mn}_y\text{Co}_z)\text{O}_2$ grains. These grains are made of the same chemical elements, but in different ratios $x:y:z$, often abbreviated as NMCxyz. We have used NMC111, NMC811, and NMC622 (i.e., Ni∶Mn∶Co ratios 1∶1∶1, 8∶1∶1, and 6∶2∶2, respectively), in order to explore the possibility of identifying different compositions based on their spectral responses. NMC is used as an active cathode material for lithium-ion batteries and can be found in a wide range of electronic devices, from mobile phones and laptops to electric cars. However, research is still underway to understand the relationship between microstructure and electrochemistry [18,19], including its dependence on metal ratios and their different aging characteristics [20,21].

The sample was placed ∼21.5 mm downstream of the FZP to produce a probe diameter ranging from 15 to 11 μm between 7.6 and 8.6 keV (see also Supplementary Material [22]). The sample was scanned through the probe in a 20 × 30 grid with 1 μm steps, while recording the diffraction patterns statically at each step for 5 s. The 2D acquisition was repeated at 16 different angles within a 180° range. The total 3D scan duration, including overheads, was 16.5 h.

The data processing was performed in three stages. First, the raw detector frames were analyzed to produce a list of photons with floating point energy and location. This list was converted into a spectral ptychographic dataset with 208 eV wide energy bins, using a sliding window approach with an 80 eV step size. This bin width resulted in approximately 3.6×10^4 photons per diffraction pattern per energy bin, which gave a good balance between ptychographic reconstruction quality through photon statistics, and energy resolution.

Second, for 13 such energy bins, the ptychographic reconstruction of each of the 16 angular projections was performed in PtyREX [23], which is an implementation of the extended ptychographical iterative engine (ePIE) algorithm [24]. PtyREX can reconstruct all the energies in parallel, which provides a remarkable reduction of reconstruction time. No detector upsampling [8] was performed, unlike in [5], where the probe size variation was much larger. For one of these angular projections, the sample's attenuation and phase as well as the probe modulus are shown in Supplementary Material [22] for all 13 energy bins. Two of those energy bins, at the same projection angle, are also shown in Fig. 3: one energy below the Ni K-edge (center energy $E_b = 8167$ eV) and one above it (center

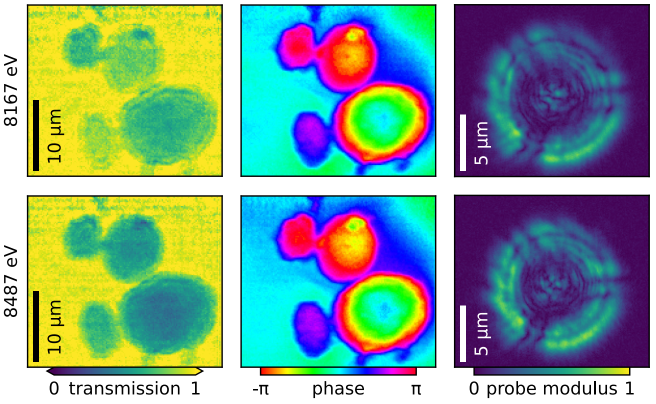

FIG. 3. Normalized transmission image, phase image, and probe modulus of a single tomographic projection above and below the Ni K-edge, taken in a single broadband ptychographic acquisition. The Ni K-edge, affecting all four particles to varying degrees, is visible in the transmission images. The shadow of the central stop with fins is visible in the probe modulus. Images have been interpolated to match in pixel size.

energy $E_a = 8487$ eV). The same energy bins were used to do two tomographic reconstructions. For each of the complex ptychographic reconstructions at both energies, the real part of the negative logarithm was taken to obtain $\mu(E)t$, the product between the local average attenuation coefficient and projected thickness, for each pixel. They were normalized by subtracting the mean value of a region of air.

Finally, the stack of ptychographic images for both energies was processed through independent tomographic reconstructions. Ptychographic reconstructions suffer from an inherent lateral shift ambiguity, causing the sample to appear to move around between angles, and between energies. To realign the projections we used the joint iterative reconstruction and reprojection approach developed by Gursoy *et al.* [25] as implemented in Tomopy [26], for 30 simultaneous iterative reconstruction technique (SIRT) [27] iterations. The projections were first blurred with a Gaussian kernel of $\sigma = 1$ pixel for this realignment step, to reduce the influence of noise. The resulting shift for each blurred projection was extracted and applied to the original projections. A 3D volume was generated from these newly aligned projections using 20 iterations of the SIRT algorithm [27], for each of the two selected energy bins. The higher energy tomogram was trigonometrically resampled to match the larger pixel size of the lower energy tomogram, inherent to the ptychographic reconstruction algorithm, using the using the fractional Fourier transform [28] (also called Chirp-Z transform). The two tomograms were then registered using phase cross-correlation [29], again using an intermediate temporary blurring operation ($\sigma = 4$). Tomographic reconstruction artifacts in the empty region due to the limited number of acquired angles were masked out for both energies, with a mask created by thresholding a blurred version ($\sigma = 6$) of the lower energy tomogram.

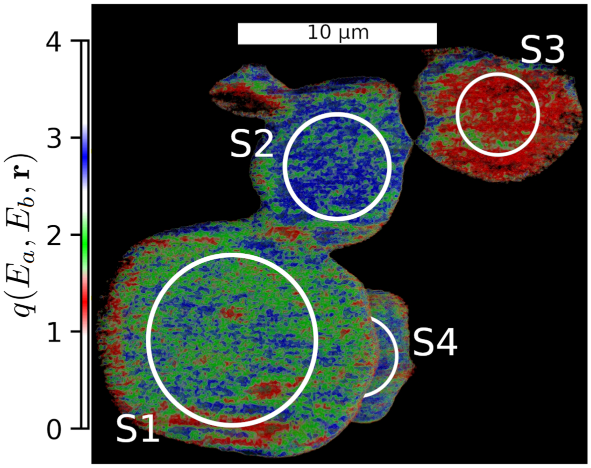

FIG. 4. Volume rendering of $q(E_a, E_b, \boldsymbol{r})$, with cut-through. $q(E_a, E_b, \boldsymbol{r})$ is the retrieved ratio between the attenuation coefficient above ($E_a = 8487$ eV) and below ($E_b = 8167$ eV) the Ni K-edge for each voxel. The color map is designed to highlight matches to the theoretical prediction. Red, green, and blue are used for NMC111, NMC622, and NMC811, respectively. The white circles represent the spherical volumes used to calculate the mean values $\bar{q}_S$ in Table I. A video of this cut-through volume rendering is available in Supplementary Material [22].

The pointwise voxel ratio $q(E_a, E_b, \boldsymbol{r})$ between the higher and lower energy tomogram was then calculated for the two energies above and below the Ni K-edge:

$$q(E_a, E_b, \boldsymbol{r}) = \frac{\mu(E_a, \boldsymbol{r})}{\mu(E_b, \boldsymbol{r})}. \tag{1}$$

The values of $q(E_a, E_b, \boldsymbol{r})$ are characteristic for each NMC composition and can be theoretically predicted. In order to compare them with the experiment, detection uncertainty has been taken into account (see Appendix A). Figure 4 shows the variation of $q(E_a, E_b, \boldsymbol{r})$ in a 3D rendering of the imaged particles using a color map based on the theoretical values, allowing for identification of the NMC grains by their color. A video of this 3D rendering is available in Supplementary Material [22]. The theoretical predictions are also reported in Table I.

$q(E_a, E_b, \boldsymbol{r})$ was blurred slightly in space ($\sigma = 1$) to create $q_{\text{blur}}(E_a, E_b, \boldsymbol{r})$. The mean of $q_{\text{blur}}(E_a, E_b, \boldsymbol{r})$,

TABLE I. Experimental and theoretical values of $\bar{q}_S(E_a = 8487\ \text{eV}, E_b = 8167\ \text{eV})$, allowing identification of different ratios xyz of $\text{N}_x\text{M}_y\text{C}_z$. The errors on the experimental values are estimated from the standard deviation.

Volume	Ratio $\bar{q}_S$	Identified as	Theoretical value
S_1	2.00 ± 0.31	NMC622	1.91
S_2	2.8 ± 0.5	NMC811	2.83
S_3	1.28 ± 0.21	NMC111	1.28
S_4	2.7 ± 0.5	NMC811	2.83

$$\bar{q}_S(E_a, E_b) = \langle \{ q_{\mathrm{blur}}(E_a, E_b, \boldsymbol{r}) | \boldsymbol{r} \in S \} \rangle, \qquad (2)$$

within four spherical volumes S_1, S_2, S_3, S_4 shown in Fig. 4, is calculated and listed in Table I. In Supplementary Material [22], a similar procedure is performed on a single 2D projection by using a relative absorption spectrum across the 13 bins in the full energy range between 7.6 keV and 8.6 keV. In Table I the different compositions are identifiable from the $\bar{q}_S$ values. The relatively high error in $\bar{q}_S$ finds its origin in the low number of tomographic projection angles and a low count rate resulting in high photon Poisson noise, potentially aggravated by the relatively large bandwidth within a single ptychographic reconstruction (see also Appendix C).

The spectral bandwidth that could be accepted by the experiment could easily cover the Co K-edge (7709 eV) as well, thanks to the smaller FZP. However, during the acquisition a slight drift of the OSA occurred, and, while this did not affect the probes above and below the Ni edge, it caused the OSA to clip the probe below the Co edge, since there it is largest. As a result, the reconstruction below the Co edge was compromised and could not be used for elemental analysis.

To the best of our knowledge, this is the first demonstration of hyperspectral x-ray ptychotomography, at a synchrotron and in general. Since synchrotron sources offer significantly more flux than the detector can handle, in this experiment the flux was reduced to match the maximum acquisition rate of the SLcam hyperspectral detector. Arguably, an energy scan acquisition at a synchrotron with a standard photon counting detector would have been faster. Indeed, the proposed scheme aims to target laboratory applications of ptychography. With 4.7×10^4 detected photon counts in an empty position of the scan, and the setup geometry, we can find the brilliance of the probe for this experiment to be 5.3×10^{14} photons $\mathrm{s}^{-1}\,\mathrm{mm}^{-2}\,\mathrm{mrad}^{-2}$ per 0.1% relative bandwidth. However, the coherence area was orders of magnitude larger than necessary. Therefore, we can define an *effective* brilliance (see Appendix B), which in this experiment was much lower, approximately 7.7×10^{10} photons $\mathrm{s}^{-1}\,\mathrm{mm}^{-2}\,\mathrm{mrad}^{-2}$ per 0.1% relative bandwidth. This brilliance is comparable to state-of-the-art laboratory sources such as [30]. A source like this has been used in a proof-of-concept x-ray ptychography experiment [31], but only in 2D and without enabling a spectral reconstruction. While spectral 2D ptychographic reconstructions have been demonstrated with laboratory data, these were limited to the visible to extreme ultraviolet range and relied on energy scanning [32] or on spectra with distinct peaks [33,34], which allows for algorithmic disentanglement [35] rather than requiring a hyperspectral detector. As such, the proposed method can represent an important leap in the process of translating x-ray coherent diffraction imaging from the synchrotron to the laboratory, as it allows one to use the continuous spectrum more efficiently by getting rid of the monochromator. This extra spectral information is valuable even when the elemental characterization is not required, especially when combined with specialized reconstruction algorithms. Compared to conventional high-resolution laboratory x-ray microscopy, the proposed method provides phase contrast as an additional imaging modality, which is beneficial for weakly absorbing samples such as those found in biology. Furthermore, the principle of low chromaticity optics and large numerical aperture can be extended to other hyperspectral detectors such has the HEXITEC MHz [36] and the Mönch [37], which can deal with higher flux and improve the potential for single acquisition broadband ptychography at synchrotron facilities. Given an acquisition time that approaches that of energy scanning, we gain the additional benefits that the diffractograms of different energies are inherently taken at the same time and position, and that the setup is free of any mechanical instabilities due to the monochromatizing optics.

In conclusion, by designing a broadband ptychography setup based on a low chromaticity small diameter FZP, we have significantly broadened the spectrum that can be covered in a single acquisition. Furthermore, this has increased the effective acquisition rate to 4.5 $\mathrm{s}\,\mu\mathrm{m}^{-2}$, 8 times faster than in [5], allowing the acquisition of a ptychotomographic dataset with a hyperspectral detector. In this work, we applied the method to discriminate between three different NMC particles by looking at the Ni absorption edge. In spite of the small number of projection angles, the reconstruction was accurate enough to detect differences in relative elemental concentration. While performed at a synchrotron, this chromaticity minimizing setup has great potential for laboratory ptychography.

Acknowledgments—The authors acknowledge Fonds Wetenschappelijk Onderzoek (FWO-Flanders) for Research Project G030220 and SBO Project 3179I12018, Interreg Vlaanderen-Nederland for Smart*Light 2.0 project, Ghent University Special Research Fund (BOF) for Grant No. BOF/STA/202202/011, the Engineering and Physical Sciences Research Council (EPSRC) for the New Investigator Award No. EP/X020657/1, and the German ministry (BMWI, BMWK, BMWE) project Hibrain 30ETE039G. Diamond Light Source is acknowledged for the funding and beam time provided under proposal MG34164-1. Matt Spink and Lisa Caboor are acknowledged for their assistance with sample preparation.

[1] J. M. Rodenburg, A. C. Hurst, A. G. Cullis, B. R. Dobson, F. Pfeiffer, O. Bunk, C. David, K. Jefimovs, and I. Johnson, Hard-x-ray lensless imaging of extended objects, Phys. Rev. Lett. **98**, 034801 (2007).

[2] F. Pfeiffer, X-ray ptychography, Nat. Photonics **12**, 9 (2018).

[3] J. Miao, R. L. Sandberg, and C. Song, Coherent x-ray diffraction imaging, IEEE J. Sel. Top. Quantum Electron. **18**, 399 (2012).

[4] T. Aidukas, N. W. Phillips, A. Diaz, E. Poghosyan, E. Müller, A. F. J. Levi, G. Aeppli, M. Guizar-Sicairos, and M. Holler, High-performance 4-nm-resolution x-ray tomography using burst ptychography, Nature (London) **632**, 81 (2024).

[5] D. J. Batey, S. Cipiccia, F. Van Assche, S. Vanheule, J. Vanmechelen, M. N. Boone, and C. Rau, Spectroscopic imaging with single acquisition ptychography and a hyperspectral detector, Sci. Rep. **9**, 12278 (2019).

[6] A. M. Wise, J. N. Weker, S. Kalirai, M. Farmand, D. A. Shapiro, F. Meirer, and B. M. Weckhuysen, Nanoscale chemical imaging of an individual catalyst particle with soft x-ray ptychography, ACS Catal. **6**, 2178 (2016).

[7] F. Bardelli, F. Brun, S. De Panfilis, P. Cloetens, S. Capella, E. Belluso, D. Bellis, A. Di Napoli, and A. Cedola, Chemo-physical properties of asbestos bodies in human lung tissues studied at the nano-scale by non-invasive, Toxicol. Lett. **348**, 18 (2021).

[8] D. J. Batey, T. B. Edo, C. Rau, U. Wagner, Z. D. Pešić, T. A. Waigh, and J. M. Rodenburg, Reciprocal-space up-sampling from real-space oversampling in x-ray ptychography, Phys. Rev. A **89**, 043812 (2014).

[9] W. Stolp, S. Cipiccia, D. Batey, and M. N. Boone, Optics for broadband x-ray ptychography (to be published).

[10] L. Loetgering, X. Liu, A. C. C. D. Beurs, M. Du, G. Kuijper, K. S. E. Eikema, and S. Witte, Tailoring spatial entropy in extreme ultraviolet focused beams for multispectral ptychography, Optica **8**, 130 (2021).

[11] D. Batey, S. Cipiccia, X. Shi, S. Williams, K. Wanelik, A. Wilson, S. Pérez-Tamarit, P. Cimavilla, M. A. Ródriguez-Pérez, and C. Rau, Coherence branch at I13, DLS: The multiscale, multimodal, ptycho-tomographic end station, Microsc. Microanal. **24**, 40 (2018).

[12] D. A. Mossessian and P. A. Heimann, Characterization of ALS undulator radiation—high K, taper, and the near field effect, Rev. Sci. Instrum. **66**, 5153 (1995).

[13] I. Ordavo *et al.*, A new pnCCD-based color x-ray camera for fast spatial and energy-resolved measurements, Nucl. Instrum. Methods Phys. Res., Sect. A **654**, 250 (2011).

[14] A. Bjeoumikhov, G. Buzanich, N. Langhoff, I. Ordavo, M. Radtke, U. Reinholz, H. Riesemeier, O. Scharf, H. Soltau, and R. Wedell, The SLcam: A full-field energy dispersive x-ray camera, J. Instrum. **7**, C11008 (2012).

[15] G. F. Knoll, *Radiation Detection and Measurement* (John Wiley & Sons, New York, 2010).

[16] M. N. Boone, J. Garrevoet, P. Tack, O. Scharf, D. P. Cormode, D. Van Loo, E. Pauwels, M. Dierick, L. Vincze, and L. Van Hoorebeke, High spectral and spatial resolution x-ray transmission radiography and tomography using a Color X-ray Camera, Nucl. Instrum. Methods Phys. Res., Sect. A **735**, 644 (2014).

[17] F. Van Assche, S. Vanheule, L. Van Hoorebeke, and M. N. Boone, The spectral x-ray imaging data acquisition (SpeXIDAQ) framework, Sensors (Switzerland) **21**, 563 (2021).

[18] T. M. M. Heenan, A. Wade, C. Tan, J. E. Parker, D. Matras, A. S. Leach, J. B. Robinson, A. Llewellyn, A. Dimitrijevic, R. Jervis, P. D. Quinn, D. J. L. Brett, and P. R. Shearing, Identifying the origins of microstructural defects such as cracking within Ni-Rich NMC811 cathode particles for lithium-ion batteries, Adv. Energy Mater. **10**, 2002655 (2020).

[19] T. M. M. Heenan, A. V. Llewellyn, A. S. Leach, M. D. R. Kok, C. Tan, R. Jervis, D. J. L. Brett, and P. R. Shearing, Resolving Li-ion battery electrode particles using rapid lab-based x-ray nano-computed tomography for high-throughput quantification, Adv. Sci. **7**, 2000362 (2020).

[20] C. Zhan, T. Wu, J. Lu, and K. Amine, Dissolution, migration, and deposition of transition metal ions in Li-ion batteries exemplified by Mn-based cathodes—a critical review, Energy Environ. Sci. **11**, 243 (2018).

[21] L. R. Brandt, J.-J. Marie, T. Moxham, D. P. Förstermann, E. Salvati, C. Besnard, C. Papadaki, Z. Wang, P. G. Bruce, and A. M. Korsunsky, Synchrotron x-ray quantitative evaluation of transient deformation and damage phenomena in a single nickel-rich cathode particle, Energy Environ. Sci. **13**, 3556 (2020).

[22] See Supplemental Material at http://link.aps.org/supplemental/10.1103/kbrf-gb9c for a video of the 3D rendering, ptychographic reconstructions across the whole energy range, and a full absorption spectrum of the different particles.

[23] D. Batey, Ptychographic imaging of mixed states, Ph.D. thesis, University of Scheffield, 2014.

[24] A. M. Maiden and J. M. Rodenburg, An improved ptychographical phase retrieval algorithm for diffractive imaging, Ultramicroscopy **109**, 1256 (2009).

[25] D. Gürsoy, Y. P. Hong, K. He, K. Hujsak, S. Yoo, S. Chen, Y. Li, M. Ge, L. M. Miller, Y. S. Chu, V. De Andrade, K. He, O. Cossairt, A. K. Katsaggelos, and C. Jacobsen, Rapid alignment of nanotomography data using joint iterative reconstruction and reprojection, Sci. Rep. **7**, 11818 (2017).

[26] D. Gürsoy, F. De Carlo, X. Xiao, and C. Jacobsen, TomoPy: A framework for the analysis of synchrotron tomographic data, J. Synchrotron Radiat. **21**, 1188 (2014).

[27] P. Gilbert, Iterative methods for the three-dimensional reconstruction of an object from projections, J. Theor. Biol. **36**, 105 (1972).

[28] D. H. Bailey and P. N. Swarztrauber, The fractional Fourier transform and applications, SIAM Rev. **33**, 389 (1991).

[29] M. Guizar-Sicairos, S. T. Thurman, and J. R. Fienup, Efficient subpixel image registration algorithms, Opt. Lett. **33**, 156 (2008).

[30] D. H. Larsson, P. a. C. Takman, U. Lundström, A. Burvall, and H. M. Hertz, A 24 keV liquid-metal-jet x-ray source for biomedical applications, Rev. Sci. Instrum. **82**, 123701 (2011).

[31] D. J. Batey, F. Van Assche, S. Vanheule, M. N. Boone, A. J. Parnell, O. O. Mykhaylyk, C. Rau, and S. Cipiccia, X-ray ptychography with a laboratory source, Phys. Rev. Lett. **126**, 193902 (2021).

[32] P. Zhang, J. Zhao, B. Lin, X. Wu, and G. Cui, Hyperspectral microscopy imaging based on Fourier ptychographic microscopy, J. Opt. **24**, 055301 (2022).

[33] B. Zhang, D. F. Gardner, M. H. Seaberg, E. R. Shanblatt, C. L. Porter, R. Karl, C. A. Mancuso, H. C. Kapteyn, M. M. Murnane, and D. E. Adams, Ptychographic hyperspectral

spectromicroscopy with an extreme ultraviolet high harmonic comb, Opt. Express **24**, 18745 (2016).

[34] L. Loetgering, S. Witte, and J. Rothhardt, Advances in laboratory-scale ptychography using high harmonic sources [Invited], Opt. Express **30**, 4133 (2022).

[35] D. J. Batey, D. Claus, and J. M. Rodenburg, Information multiplexing in ptychography, Ultramicroscopy **138**, 13 (2014).

[36] L. Jones, S. Bell, B. Cline, T. Gardiner, M. Hart, M. Prydderch, P. Seller, M. Veale, and M. Wilson, Spectroscopic x-ray imaging at MHz frame rates—the HEXITECMHz ASIC, J. Instrum. **17**, C10012 (2022).

[37] A. Bergamaschi *et al.*, The MÖNCH detector for soft x-ray, high-resolution, and energy resolved applications, Synchrotron Radiat. News **31**, 11 (2018).

[38] B. L. Henke, E. M. Gullikson, and J. C. Davis, X-ray interactions: Photoabsorption, scattering, transmission, and reflection at $E = 50–30,000$ eV, $Z = 1–92$, At. Data Nucl. Data Tables **54**, 181 (1993).

[39] J. Spence, U. Weierstall, and M. Howells, Coherence and sampling requirements for diffractive imaging, Ultramicroscopy **101**, 149 (2004).

[40] D. Paganin, *Coherent X-Ray Optics* (Oxford University Press, New York, 2006).

[41] B. Lai, W. B. Yun, D. Legnini, Y. Xiao, J. Chrzas, P. J. Viccaro, V. White, S. Bajikar, D. Denton, F. Cerrina, E. Di Fabrizio, M. Gentili, L. Grella, and M. Baciocchi, Hard x-ray phase zone plate fabricated by lithographic techniques, Appl. Phys. Lett. **61**, 1877 (1992).

End Matter

Appendix A: Estimating detection uncertainty—To estimate uncertainties in the photon energy detection process, first the predicted attenuation coefficient $\mu(E)$ for each NMC particle was calculated from the attenuation coefficients of its constituent elements, which were taken from the database of the Center for X-Ray Optics at Lawrence Berkeley National Laboratory [38]. These NMC $\mu(E)$ were then convolved with a 180 eV FHMW Gaussian kernel and a 208 eV wide rectangular function, representing, respectively, the SLcam energy resolution at 8.3 keV and the chosen energy bin width. These convolved versions of $\mu(E)$, plotted in Fig. 2(c), were then used to calculate the theoretically predicted ratio $q(E_a, E_b, \boldsymbol{r})$, one for each NMC composition.

Figure 2(b) shows an approximation of the distribution of counts that are actually selected for reconstruction. This is done by combining the two kernels, through convolution, and multiplying the result with the high-resolution recorded spectrum.

Appendix B: Calculation of effective brilliance—In this experiment, the secondary source slits were closed to create a relatively small surface area A_s, with the aim to reduce photon counts without affecting the spectrum. This procedure, however, increases the coherence area,

$$A_c = \frac{z^2\lambda^2}{A_s}, \tag{B1}$$

where z is the distance from the source to the sample and λ the wavelength of the radiation. The true brilliance is conventionally defined as

$$B_{\text{true}} = 10^{-3}\frac{NE}{T\sigma^2 A_s \Delta E}, \tag{B2}$$

where N is the number of photons passing in T time through an area that subtends a solid angle σ^2 at the source, which has a relative spectral bandwidth $\Delta E/E$. Thus, in this scenario, with $N \propto A_s$, the true brilliance remains constant while decreasing A_s.

However, if

$$A_c \gg A_{\text{eff}} = (\sigma z)^2, \tag{B3}$$

where A_{eff} is the area containing the flux we effectively capture with our FZP and use in our experiment, we are essentially "wasting" coherence; thus, we can say that our true brilliance is not fully *effective*. If our source had been more similar to a lab source, larger but proportionally less intense with the same total flux, A_c would have been smaller. But as long as $A_c \geq (\sigma z)^2$ [39], we would still be able to do the same experiment in the same way. To compare different sources fairly, we can, thus, define an effective brilliance,

$$B_{\text{eff}} = B_{\text{true}}\frac{A_{\text{eff}}}{A_c}. \tag{B4}$$

If we fill in these three terms, we arrive at

$$B_{\text{eff}} = 10^{-3}\frac{NE}{T\Delta E\lambda^2} = 10^{-3}\frac{N}{T\lambda\Delta\lambda}. \tag{B5}$$

Now using for ΔE the energy bin width used in our reconstructions and N/T the number of collected counts per exposure time, we can find this effective brilliance to be roughly 1.8×10^{10} photons $\text{s}^{-1}\,\text{mm}^{-2}\,\text{mrad}^{-2}$ per 0.1% relative bandwidth, depending on where we are in the spectrum. For the comparison with a laboratory source, we assume that the source has a spectrum similar to Fig. 2(a) already. We do correct for the FZP efficiency, which is theoretically calculated to be 22% [40], a number that conforms to experimentally verified values [41]. This way we end up with an equivalent required lab source brilliance of 8.1×10^{10} photons $\text{s}^{-1}\,\text{mm}^{-2}\,\text{mrad}^{-2}$ per 0.1% relative bandwidth.

Appendix C: Partial temporal coherence—It should be noted that in the presence of partial temporal coherence, the smallest resolvable feature size d_{min} is limited by the bandwidth [39]:

$$d_{\mathrm{min}} > D_{\mathrm{probe}} \frac{\Delta E}{E}, \tag{C1}$$

where D_{probe} is the probe diameter and E and ΔE are the energy and energy bandwidth, respectively. Therefore, both the energy resolution and our chosen bin width can pose a limit on the smallest resolvable feature size that is larger than the usual Bragg limit, and this is also the case for the experiment reported here. For example, with a 11.7 μm wide probe at 8.4 keV, if we interpret ΔE as the 180 eV energy resolution of our detector, this limit for d_{min} is 251 nm, which is larger than the smallest resolvable feature size determined by the Bragg angle in our geometry (182 nm). If we use instead for ΔE the FWHM resulting from the energy resolution and 208 bin selection, which is approx. 240 eV, d_{min} is 335 nm.